1 **Macrophage transactivation for chemokine production identified as a negative**

2 **regulator of granulomatous inflammation using agent-based modeling.**

3

4 Daniel Moyo[1,2], Lynette Beattie[1*], Paul S Andrews[3], John W J Moore[1], Jon Timmis[3],

5 Amy Sawtell[1], Stefan Hoehme[4], Adam T. Sampson[5], Paul M Kaye[1]

6

7 [1.] Centre for Immunology and Infection, Department of Biology and Hull York

8 Medical School, University of York, UK.

9 [2.] Department of Computer Science, University of York, UK.

10 [3.] Department of Electronics, University of York, UK and SimOmics Ltd, York. U.K.

11 [4.] Institute for Computer Science, University of Leipzig, Germany

12 [5.] Division of Computing and Mathematics, Abertay University, Dundee, UK.

13

14 ***Current address: Doherty Institute, University of Melbourne, Australia.

15 **Key words:** Kupffer cells**;** granulomas; inflammation; *Leishmania*; NKT cells;

16 agent-based modeling; computational immunology; liver

17

18   **Abstract**

19   Cellular activation *in trans* by interferons, cytokines and chemokines is a commonly

20   recognized mechanism to amplify immune effector function and limit pathogen

21   spread. However, an optimal host response also requires that collateral damage

22   associated with inflammation is limited.   This may be particularly so in the case of

23   granulomatous inflammation, where an excessive number and / or excessively florid

24   granulomas can have significant pathological consequences. Here, we have combined

25   transcriptomics, agent-based modeling and *in vivo* experimental approaches to study

26   constraints on hepatic granuloma formation in a murine model of experimental

27   leishmaniasis. We demonstrate that chemokine production by non-infected Kupffer

28   cells in the *Leishmania donovani*-infected liver promotes competition with infected

29   KCs for available iNKT cells, ultimately inhibiting the extent of granulomatous

30   inflammation.   We propose trans-activation for chemokine production as a novel

31   broadly applicable mechanism that may operate early in infection to limit excessive

32   focal inflammation.

33

34

Introduction

Immune responses are commonly initiated by localized infectious insult and multiple mechanisms have evolved to allow spread of host effector responses to meet the challenge of pathogen containment. In the late 1950's, seminal studies by Isaacs and Lindenmann defined how "interferons' amplified local cellular resistance following virus infection [1, 2]. A decade later, Mackaness described cross protective cellular immunity mediated via T cell cytokine-dependent macrophage activation [3]. More recently, cytokine-and chemokine- mediated amplification of host protective immunity has been described across a spectrum of responses driven by both innate lymphoid cells and via conventional T cells [4-9]. Whilst serving to eliminate pathogens more effectively, a potentially undesirable consequence of amplifying immune effector responses is immunopathology, collateral damage induced by an over-zealous drive towards inflammation. Hence, an equally impressive array of "regulatory" or "suppressive" mechanisms have been defined that serve to limit immunopathology, and that suggest an evolutionary balance between pathogen elimination and host survival [10-12].

Granulomatous inflammation represents an extreme form of focal inflammation, often initiated around pathogens or foreign bodies that pose a formidable challenge for immune clearance. Granulomas are a hallmark of the immunopathology of many human infectious diseases including tuberculosis [13, 14], schistosomiasis [15]and leishmaniasis [16]. Whilst granuloma formation may provide means for containment and be host beneficial, excessive granuloma formation, numerically or in terms of individual granuloma size can lead to severe pathological consequences. Hence,

59   mechanisms for limiting the exuberance of the granulomatous response through late

60   acting regulatory pathways are also well described in the literature [17-20]. However,

61   the question of whether additional regulatory mechanisms operate at the earliest

62   stages of granuloma initiation and prevent or limit over-exuberant granuloma

63   formation has not been previously addressed.

64

65   Experimental visceral leishmaniasis, resulting from infection of mice with the Kupffer

66   cell (KC) tropic parasite *Leishmania donovani*, has provided a highly tractable tool to

67   study the initiation of granulomatous pathology in the hepatic microenvironment.

68   Following infection of mice with *L. donovani*, infected KCs transiently release the

69   chemokines CCL1, CCL2 and CXCL10 in a T cell-independent manner, whereas

70   sustained expression of CXCL10 is dependent upon IFNγ production by invariant

71   NKT (iNKT) cells [21]. IFNγ production by iNKT cells is in turn costimulated by

72   ligation of CD47 on NKT cells by signal regulatory protein alpha (SIRPα) expressed

73   on KCs, providing positive feedback for sustained iNKT cell recruitment and KC

74   activation [22].   A similar role for CXC chemokines in recruiting hepatic NKT cells

75   has been observed in other models of liver infection / inflammation [23, 24]. For

76   example, CXCL9 produced by KCs following infection with the bacterium *Borrelia*

77   *burgdorferi* results in CXCR3-dependent clustering of NKT cells around infected

78   KCs [25] whereas CXCR6 and its ligand CXCL16 regulate NKT cell accumulation in

79   the liver during fibrosis [26]. Hence, early recruitment of "amplifier" cells such as

80   NKT cells is a central and common theme of focal inflammation.

81

82   Examination of the kinetics of granulomatous inflammation in this model of visceral

83   leishmaniasis suggests, however, that there may be inherent limitations imposed on

84   the ability of the host to form hepatic granulomas. Notably, granuloma formation

85   proceeds asynchronously, and even many weeks after infection, fully formed

86   granulomas sit side by side with infected KCs that appear to have failed to stimulate

87   an inflammatory focus [16, 27]. Here, we have combined transcriptional profiling

88   and computational modeling to probe possible mechanisms that might underpin the

89   asynchronous development of granulomas in this model. We demonstrate that KC

90   chemokine production, contrary to expectations, is not restricted to infected cells

91   alone, but spreads in trans to include uninfected KCs within the infected liver. Data

92   generated using a novel agent based model (ABM) in which KCs and iNKT cells

93   interact within a spatially constrained sinusoidal network suggest that the spreading of

94   chemokine production to uninfected KCs limits the competitiveness of infected KCs

95   in terms of their ability to attract iNKT cells and initiate granuloma formation. In

96   silico experiments predicted that this competition could be overcome by increasing

97   the number of available NKT cells, a prediction borne out in vivo. Hence, our data

98   identify a new pathway that operates early in infection to limit excessive

99   inflammation by introducing competition for a finite resource (i.e. iNKT cells) that is

100   needed for granuloma initiation.

101

Materials and Methods

102

Mice and parasites.

103

104   C57BL6 mice were obtained from Charles River (UK). mT/mG [28] and LysMcre

105   [29] mice have been previously described. Mice were bred and housed under specific

106   pathogen-free conditions and used at 6-12 weeks of age. The tandom Tomato

107   fluorescent protein expressing Ethiopian strain of *Leishmania donovani* (tdTom.LV9)

108   [30] were maintained by serial passage in *Rag1*$^{-/-}$ mice. Amastigotes were isolated

109   from infected spleens, and mice were infected with 3×10^7 *L. donovani* amastigotes

110   intravenously (i.v.) via the tail vein in 200μl of RPMI 1640 (GIBCO, UK). All

111   animal procedures were approved by the University of York Animal Welfare and

112   Ethical Review Board and carried out in accordance with UK Home Office license

113   (PPL 60/4377).

114

115   *Microarray analysis*

116   As previously described [31], Kupffer cells were flow sorted (on the basis of

117   SSC/FSC and expression of CRIg, Gr-1 and F4/80) from naive mice and from

118   infected mice and KCs from infected mice were further sorted (on the basis of

119   TdTomato expression) into those containing amastigotes ("infected") and those that

120   did not ("inflamed"). A total of 64 mice were used in the microarry study, in four

121   independent infection experiments. RNA was isolated, amplified and equal amounts

122   were assayed using Agilent SurePrint G3 Gene Expression 8x60 Microarray chips.

123   Scanned data were normalized (80th percentile) and gene expression data analysed

124   using Genespring v9. Differentially expressed (DE) genes were defined using a false

125   discovery rate (FDR) of 5%. Source data is accessible from EBI Array Express (E-

126   MEXP-3877) and methodology for subsequent data analysis is described in further

127   detail elsewhere [31].

128

129   *Histological Analysis.*

130   Mice were treated with 1μg recombinant IL-15 (BioLegend) intravenously and

131   infected 3 days later. Four days post-infection, mice livers were extracted, weighed

132   then placed into 2% PFA in PBS for 2 hours, then 30% sucrose in PBS overnight.

133   Tissues were then embedded in Optimal Cutting Temperature (OCT)(Sakura) and

134   stored at -70°C until use. 10μm cryosections were fixed and labeled with Alexa647 or

135   Alexa488 conjugated F4/80 (eBioscience) and DAPI (Invitrogen) to visualize KCs

136   and cell nuclei respectively. Images were captured as 0.81μm optical slices using a

137   LSM510 confocal microscope (Zeiss). Blinded slides were imaged to score the

138   percentage of infected foci having formed a distinct inflammatory focus (greater than

139   15 cells), with imaging fields selected via tdTomato expression.

140

141   *Flow Cytometry.*

142   Livers were homogenized and mononuclear cells prepared as previously described

143   [30]. Cells were incubated with anti-CD16/32 and then labeled with NK1.1, CD3,

144   B220 and CD1d tetramer (a kind gift from V. Cerundulo) to identify T, NK and NKT

145   cells. Samples were analyzed using a CyAn flow cytometer with Summit software

146   (DAKO). Autofluorescent events and dead cells were excluded from analysis by

147   gating on unused fluorescent channels and LIVE/DEAD fixable dead cell stain

148   (Invitrogen) respectively.

149

150   *Parameterizing and Calibrating the Simulation.*

151   A full summary of the biological data available that was used to calibrate the

152   simulation is listed in **Table S1**. The entire list of baseline simulation parameters is

153   found in **Tables S3**. Full details of parameterization and calibration of the simulation

154   are provided in the **Supplemental Experimental Procedures**.

155

156   *Statistical Analysis*.

157   When quantifying granulomas, experimental data are expressed as mean ± SEM for

158   each group of 5 mice from two independent experiments, and statistical analyses

159   performed using two-tailed paired Student t-tests. All tests used 95% confidence

160   intervals. Simulation data non-normality was determined using the D'Agostino and

161   Pearson test, and non-normal simulation data was analyzed using either Wilcoxon

162   signed-rank or Kolmogorov-Smirnov tests where appropriate. Aleatory analysis was

163   used to determine the minimum number of simulation results required to mitigate

164   stochastic uncertainty (see **Figure S4**). Latin-hypercube sensitivity analysis was

165   facilitated by using the Spartan tool for understanding uncertainty in simulations [32].

166

167   **Results**

168   *Chemokine production by KCs in mice infected with L. donovani*

169   Both chemokines and iNKT cells are central to the initiation of granulomatous

170   inflammation following *L. donovani* infection. In order to gain insight into the

171   production of chemokines involved in KC-directed recruitment of NKT cells, we used

172   transcriptional profiling of KCs isolated from mice infected with *L. donovani* as

173   previously described [31]. Following infection of mice with Td-tomato transgenic *L.*

174   *donovani*, approx. 20% of the KC population are infected with amastigotes. We

175   isolated KCs from infected mice and sort purified these KCs on the basis of whether

176   they contained intracellular amastigotes ("infected') or not (herein referred to as

177   "inflamed" to denote their exposure to inflammatory signals *in vivo*) [31]. As shown

178   in **Figure 1A**, KCs from infected mice expressed a variety of chemokines when

179   compared to KCs isolated from naïve mice. At 2h post infection (p.i.), enhanced

180   accumulation of mRNAs for *Cxcl1*, *Cxcl2*, *Cxcl3* and *Cxcl5*, as well as *Ccl3* and *Ccl4*,

181   was evident (determined as differentially expressed using a 5% FDR). This

182   transcriptional response was transient, in keeping with previous studies at the level of

183   whole liver tissue [21]. Rapid secretion of chemokines in response to *L. donovani*

184   infection can also be inferred from studies in which G-protein coupled receptor

185   signaling was abrogated by pertussis toxin [22]. A suite of inducible chemokines,

186   including *Cxcl9*, *Cxcl10*, *Ccl8* and *Ccl12* showed enhanced mRNA accumulation at

187   12h p.i. (at a 5% FDR), again in keeping with data in whole liver and with previously

188   published data indicating the production of IFNγ by iNKT cells during early *L.*

189   *donovani* infection (e.g. Figure 2 in reference 22). For example, qRT-PCR

190   demonstrated sustained and elevated *Cxcl10* at 24h p.i. [33]. Similarly,

191   transcriptional profiling of the livers of infected BALB/c mice (n=4-5 per time point)

192   indicates sustained elevation of *Cxcl9* (Log_2FC compared to controls of 5.25, 5.14,

193   5.34 and 4.74 for days 15, 21, 36 and 42 p.i. respectively; FDR 0.05, $p<0.05$) and

194   *Cxcl10* (Log_2FC of 4.84, 4.92, 5.36 and 4.55, respectively; Ashwin et al, manuscript

195   in preparation).   Strikingly, there was little difference to discriminate the chemokine

196   response of infected vs. inflamed KCs, although we cannot rule out different degrees

197   of post transcriptional regulation of chemokine secretion in infected vs. inflamed KCs

198   [34]. Collectively, our data suggest that although initiated by infection, production of

199   chemokines rapidly spreads in trans throughout the liver KC network.

200

201   Chemokine induction by infected cells is thought to provide a means for focal

202   inflammation, the recruitment of additional leucocytes in an ordered manner being

203   essential for granuloma formation and the ultimate activation of macrophage host

204   defense mechanisms. However, given this argument, these data appear

205   counterintuitive. In order to try to understand how transactivation for chemokine

206   production might influence the generation of focal inflammation, and given the

207   absence of tools to selectively and directly manipulate chemokine production by

208   infected vs. uninfected KCs *in vivo*, we adopted an *in silico* experimental approach

209   conducive to testing a variety of different hypotheses (**Figure 1B and C**).

210

211   *An agent-based model of the hepatic sinusoidal microenvironment.*

212   Agent based models, where rule-driven "agents" can represent a cell or lower-scale

213   entities of interest, are naturally suited to simulating inflammation in a spatially

214   constrained environment [35-37]. To construct this environment, we used published

215   3D data describing the overall size of lobules, the average non-branched sinusoid

216   length, and the branching angles between sinusoids [38] as the basis for developing a

217   novel algorithm to generate statistically realistic liver lobule sections similar to that

218   reported recently [39]. A range of quasi-2D sinusoidal network structures, where

219   each structure can be considered as a slice through a 3D lobule, was created using a

220   multi-stage generative algorithm augmented with these data [38] (**Figure 2A**, **Movie**

221   **S1**, **Figure S1A-D** and **Table S1** and **Supplementary Experimental Procedures**).

222   The resulting networks **(Figure 2B)**, represented as graphs of nodes connected by

223   edges, serve as discrete spatial simulation environments that mimic the sinusoidal

224   structure observed in live mice imaged by 2-photon intra-vital microscopy in (mT/mG

225   x lysMcre)$_{F1}$, as previously described [30] (**Figure 2A vs. 2C**). Analysis (by Pearson

226   correlation coefficients and Kolmogorov-Smirnov tests) using 10 independently

227   generated structures indicated that variance in structure *per se* had minimal impact on

228   the results of subsequent simulations (see below).

229

230   We defined where and how cellular interactions were allowed to occur within our

231   simulation environment based on 3 different types of network node: periportal nodes,

232   located at the peripheries of the structure allow NKT cells to enter and exit the

233   simulated lobule section; regular-nodes, capable of holding a single KC and any

234   number of NKT cells; and a single centrilobular-node, representing the central vein

235   where NKT cells could exit the structure. Only NKT cells were capable of movement

236   within the structure. KCs remain immobile, as reported in early stages of infection

237   with *B. bugdorferi* [25], BCG [40] and *L. donovani* [30]. Our KC placement

238   algorithm distributes KCs in periportal, midzonal and centrilobular locations in a ratio

239   of 4:3:3, based on [41, 42]. As centrilobular KCs have reduced phagocytic capability

240   compared to periportal KCs [41], the distribution of infected KCs in our simulation is

241   65% periportal, 25% midzonal and 10% centrilobular for the purposes of

242   experimentation.

243

244   A detailed description of the model and key assumptions is provided in the

245   **Supplemental Experimental Procedures and Tables S2 and S3**. State diagrams

246   written in the Unified Modeling Language that illustrate the behaviour associated with

247   KCs and NKT cells are provided in **Figure S2**. Briefly, mechanisms of cellular

248   attraction and retention were modeled generically, since the precise function,

249   functional overlap, and interaction between distinct chemokines has yet to be fully

250   elucidated. For the purposes of the current abstraction, we refer to the chemokines as

251   attractive and retentive, being independent and quantitatively distinct and with

252   discrete areas of influence. The simulation was constructed to allow both a minimum

253   and a maximum diffusion distance to be parameterized for all chemo-attractants

254   produced by KCs. NKT cells traverse the sinusoidal network at 10-20μm/min with a

255   random walk behavior [25], with no enforcement of directionality unless under the

256   attractive influence of KC-derived chemokines. Strength of attraction is modeled as a

257   function of distance from the source KC. Upon interaction with infected KCs, NKT

258   cells produce IFNγ (as a representation of all macrophage-activating cytokines)

259   following cognate receptor engagement [22], facilitating KC activation and NKT cell

260   arrest [25, 43]. Our previous data on SIRPα-CD47 has suggested that cognate

261   receptor-ligand interactions also regulate NKT cell retention on infected KCs, with

262   the induced expression of SIRPα after infection being preferentially but not

263   exclusively observed on infected KCs [22]. In our model, this interaction is used to

264   represent a cognate retention signal, but this reflects an abstraction of what may be

265   potentially much more complex interactions. The amplification of KC derived

266   attractive chemokines through this process can lead to the accumulation of multiple

267   NKT cells at a given KC (referred to here as "inflammatory foci"). It is assumed that

268   through the sum of all KC-NKT cell interactions within an inflammatory focus, a

269 threshold for granuloma formation and the subsequent recruitment of additional

270 leucocytes associated with maturing granulomas (including B cells, T cells,

271 monocytes and NK cells) is reached, but these cells and processes are not explicitly

272 modeled. We have also not modeled the ultimate microbicidal activity of these

273 granulomas.

274

275 *Parasite Induced Activation of Infected KCs with/without Bystander Chemokine*

276 *production by Uninfected KCs.*

277 Two experimental scenarios were devised to investigate the influence of varying both

278 infected and inflamed KC function. Scenario 1 (**Figure 1B**) was constructed to restrict

279 chemokine production to infected KCs only, and scenario 2 (**Figure 1C**) to

280 investigate the impact of transactivation of KC for chemokine production. As KC

281 activation of NKT cells is optimal in the presence of cognate interactions [22], our

282 model assumes these are a requirement for retention; hence only infected KCs can

283 generate stable inflammatory foci, and these foci, for the purposes of the model, are

284 composed only of NKT cells and KCs.   In contrast, inflamed KCs in scenario 2 might

285 act as potential competitors for available NKT cells, being able to attract but not

286 retain them.   Although this model can be used to probe a variety of different potential

287 questions related to the initiation of granuloma formation (see Discussion), we focus

288 here on a factorial analysis that involved simultaneously modifying the simulation

289 parameters related to chemokine diffusion distance, time required to activate KCs,

290 and time for KCs to reach maximal chemokine production.

291

292   Firstly, we quantified the influence of distance from effect on attraction. Factorial

293   analysis, modifying the maximum diffusion distance of chemokine, showed that

294   greater chemokine diffusion distance leads to increased percentages of infected KCs

295   forming inflammatory foci in both scenarios (**Figure 1B** and **C**), whether those foci

296   were qualified as containing 4, 6 or 8 NKT cells. However, our simulation predicted

297   diminishing returns when increasing maximum diffusion past ~120μm (**Figure S1E**).

298   Thus, significant differences (P=≤0.001) were observed when comparing the

299   frequency of inflammatory foci that resulted from each increase in diffusion distance

300   against the previous distance (e.g. 20μm-30μm: P=0.001216, 30μm-40μm:

301   P=0.000019). However, when increasing from 120μm-130μm and beyond, the

302   increase in inflammatory foci was not significant (P=0.312). Interestingly, this tipping

303   point is close to the ~100μm reported as the distance of a functional chemokine

304   gradient *in vivo* [44]. These results suggest that if it were possible to selectively

305   increase chemokine diffusion via increased production (or other means) by infected

306   KCs compared to inflamed KCs, or conversely decrease chemokine diffusion by

307   inflamed KCs, infected KCs would gain competitive advantage in terms of attracting

308   NKT cells.

309

310   We next compared our two experimental scenarios in terms of total stimulation time

311   (i.e. a measure of activation) received by the entire infected KC population, and the

312   frequency of inflammatory foci formed associated with that population. **Figure 3A**

313   illustrates a response curve for scenario 1 showing the total stimulation time received

314   by all infected KCs, across a range of the two main parameters that determine KC

315   activation dynamics – the time required to activate KCs and the duration KCs remain

316   activated. When comparing this response landscape of scenario 1 with that generated

317   in scenario 2 (**Figure 3C**), there was a marked reduction in stimulation time received

318   overall by infected KCs in scenario 2 compared to scenario 1. This trend is also

319   observable when comparing the percentage of inflammatory foci, whether qualified at

320   8 NKT cells (**Figure 3B** for scenario 1 and **Figure 3D** for scenario 2) or at 4 or 6

321   NKT cells (data not shown).

322

323   Together, these results demonstrate that in comparison to chemokine production

324   restricted to infected KCs, additional chemokine production by inflamed KC

325   generates a less focused inflammatory response, measured either by frequency of

326   infected KC that form inflammatory foci, or by stimulation time received by infected

327   KCs. This result most likely reflects the liver lobule becoming saturated with

328   attractive chemokines derived from both inflamed and infected KCs in scenario 2,

329   reducing the competitiveness of infected KCs to selectively recruit NKT cells. In

330   other words, chemokine production by inflamed KC acts in a negative immune

331   regulatory manner, limiting the extent of the inflammatory response around infected

332   KCs.

333

334   *Increasing NKT Cell Numbers Overcomes Bystander Regulation.*

335   We then investigated how modifying the target of this competition affected the

336   quantity and quality of inflammatory foci generated. We hypothesized that altering

337   NKT cell frequency might result in either i) similarly abundant foci, but with each

338   being more substantive in terms of NKT cellularity, or ii) increased numbers of

339   inflammatory foci, thus overcoming the competitive effect of bystander chemokine

340   production by inflamed KCs (**Figure 4A**). Our simulation results showed that

341   increasing NKT cell numbers above the calibrated value lead to significant increases

342   in the frequency of inflammatory foci in scenario 1, a result that would be expected.

343   Strikingly, an increase in frequency of inflammatory foci was also observed to be the

344   case for scenario 2, regardless of how we qualified focus size (**Figure 4B**). For

345   example, with an increase in NKT cell availability of 2-fold, the number of

346   inflammatory foci increased 1.5-fold, whereas increasing NKT cells by 3-fold

347   doubled the frequency of inflammatory foci.

348

349   To test whether this predictive *in silico* data was also borne out *in vivo*, we treated

350   mice for 3 days with recombinant IL-15 to induce increased NKT cell proliferation

351   and survival [45] and then infected these mice with *L. donovani* and scored early

352   granuloma formation.   In uninfected mice, IL-15 treatment resulted in increased

353   numbers of NKT cells (including CD1d restricted NKT cells), NK cells, and T cells

354   (**Figure 4C-E** and **Figure S3A-D**). In infected mice, all cell types were already

355   increased in number compared to naïve mice, and the effect of IL-15 pre-treatment

356   was limited to an increase in the number of NKT cells (**Figure 4C**). Similarly, IL-15

357   pre-treatment had no effect on the relative frequency of NK cells and T cells (**Figure

358   S3B-C**) but resulted in an increase in the relative frequency of NKT cells (from 15.0

359     $\pm$ 0.1% to 17.36 $\pm$ 0.8%; n=10; P=0.0043; **Figure S3E**).

360

361   To ensure that we were scoring a biologically relevant histopathological response,

362   whilst minimizing potential longer terms effects of rIL-15 treatment, we chose to

363   score the granulomas early in their development (day 4 p.i.) and define these as

364   accumulations of 15 or more cells formed around an infected KC (not discriminating

365   between NKT cells or other mononuclear cells). Although there was significant

366   heterogeneity in size of these granulomas (**Figure 4G-H**), we found that the

367   frequency of infected KCs that formed distinct granulomas was increased ~1.5 fold in

368   mice pre-treated with IL-15 and which had a higher number of NKT cells in the liver

369   at the time of infection (P=0.0038; **Figure 4F**). Thus, treatment of mice with rIL-15,

370   even under conditions where the increase in NKT cell number is relatively modest,

371   leads to a significant enhancement in the frequency of infected KCs that can provide a

372   nidus for granuloma formation.

373

374   **Discussion**

375   Granulomas represent a specialized form of inflammation that allows for the focal

376   delivery of host effector responses and / or containment of pathogen products.

377   Whilst generally considered host beneficial, excessive granuloma formation may have

378   significant pathological consequences.   Here, we provide evidence that chemokine-

379   dependent competition between infected and uninfected KCs for iNKT cells in the

380   hepatic microenvironment acts as a natural attenuator of granuloma formation.

381

382   In models of experimental visceral leishmaniasis, granuloma formation is

383   asynchronous, limiting the extent of hepatic inflammation, but also delaying parasite

384   clearance [16, 27]. A variety of different models could explain why isolated infected

385   KCs can be found at times when other infected KCs are engaged in a fully mature

386   granulomatous response. In a model of *Mycobacterium marinarum*-induced

387   granulomas in zebrafish, macrophage migration out of the granuloma has been

388   observed [14, 46], and it is possible that infected KCs leave granulomas in mice

389   infected with *L. donovani*. However, in both *L. donovani*-induced granulomas [30]

390   and BCG-induced granulomas [40, 47] in immunocompetent mice, KCs appear to

391   retain their characteristic lack of motility. Alternatively, there may be heterogeneity

392   in KCs, a subset being more efficient in promoting granulomatous inflammation.

393   Although we had previously modeled this possibility using an early version of our

394   ABM [48], our recent studies evaluating differences between yolk-sac derived and

395   bone marrow-derived KC indicate that both are competent to form granulomas and

396   participate effectively in this response [49]. A further possibility is that granuloma

397   formation is rate limited by the availability of key amplifier cells. Experimental data

398   to date indicates that iNKT cells play this role in experimental visceral leishmaniasis

399   [22, 33, 50, 51], though we do not discount a role for other more recently identified

400   innate lymphoid cells [52, 53].

401

402   Through transcriptional profiling, we demonstrated that both inflamed and infected

403   KCs produce a variety of inducible chemokines able to attract NKT cells, suggesting

404   the possibility that uninfected as well as infected KCs could compete for this

405   resource. However, as neither the mechanisms that regulate this transactivation nor

406   experimental means to selectively regulate chemokine production by KCs are

407   currently available, we adopted a computational approach to further explore this

408   hypothesis. ABMs are well-suited towards studying tissue and cellular level

409   inflammation [35-37]. In constructing our ABM, we developed a novel algorithm for

410 creating virtual sinusoidal networks that are visually representative of liver lobule

411 sections, being defined by published statistics that captured the length between central

412 vein and portal triad, average lengths of non-branched sinusoids and sinusoid branch

413 angles [38]. This represents an improvement on similar work [39]. Our algorithm was

414 not intended to produce a fully realistic whole lobule structure, but rather we were

415 interested only in developing suitable quasi-2D vascular networks within liver lobules

416 to provide an environment for the cellular and chemokine "agents" contained in the

417 model. Similarly, whilst our ABM contained only three cellular agents (infected and

418 inflamed KCs and NKT), this abstraction was nevertheless sufficient to probe

419 previously inaccessible aspects of the underlying biology.

420

421 Our *in silico* results predicted that chemokine diffusion plays an important role in

422 regulating the formation of inflammatory foci around infected KCs, though there are

423 diminishing returns as a result of increased competition when lobules become flooded

424 with chemokines. Subsequently, our model predicted an intuitive, but nonetheless

425 previously unreported mechanism by which the production of NKT cell-attractive

426 chemokines by inflamed KCs dampens the overall inflammatory response in the liver

427 microenvironment, reducing the activation received by infected KCs. Our *in silico*

428 data also predicted that this competition could be overcome by increasing the

429 availability of NKT cells, and we were able to confirm that granuloma frequency can

430 indeed be increased *in vivo* by increasing NKT cell numbers using rIL-15. The

431 relationship between availability of NKT cells and an increase in the frequency of

432 infected KCs generating granulomas has not previously been demonstrated.

433

434   Natural killer T (NKT) cells represent a potent therapeutic target in a variety of

435   clinical settings, due to their immune adjuvant function and production of various

436   effector cytokines [54-57]. Protective immunity associated with NKT cell activation

437   has been reported in several disease settings. For example, Vα14 NKT cells activated

438   by α-galactosylceramide (α-GalCer) have been shown to inhibit the development of

439   malaria parasites in mice [58]. Similarly, in a murine model of *Mycobacterium*

440   *tuberculosis* infection, α-GalCer induced activation of NKT cells was associated with

441   reduced bacterial loads, tissue injury, and improved mouse survival [59]. Conversely,

442   NKT cells have been implicated as key drivers of liver inflammation such as chronic

443   liver injury [26]. Although our results suggest that in leishmaniasis the initiation of

444   granulomatous inflammation can be enhanced by increasing the availability of NKT

445   cells, further long-term studies would be required to determine whether the host

446   protective advantages of this intervention outweigh any possible pathological

447   consequences.

448

449   It is important to recognize that our model has been developed to address early events

450   in granuloma formation and does not take into account the potential for diversity in

451   granuloma form and function, including variations in microbicidal activity. These

452   may be regulated via other aspects of the immune response that develop over time,

453   and more complex models have been developed to address some of these issues [60].

454   Redundancy of immune regulatory pathways is a common finding and it is possible

455   that other mechanisms come into play at later stages of granuloma evolution that

456   affects the ability of Kupffer cells to recruit inflammatory cells and initiate granuloma

457   formation. The kinetics of chemokine production is also likely to be highly dynamic,

458   though in respect of CXCL9 and CXCL10, long term transcriptomic profiling

459   indicates that expression of these IFNγ-inducible chemokines is sustained for at least

460   45 days post infection (Ashwin et. al., unpublished).

461   In summary, our data argue that chemokine production by uninfected trans-activated

462   KCs provides an example of a novel negative regulatory mechanism to limit the

463   impact of over-zealous inflammatory responses that might otherwise lead to excess

464   tissue pathology. Further studies to evaluate this hypothesis in a broader context of

465   inflammation are clearly warranted.

466

472

473   **Author conflict of interest statement**

474   JT is Director of SimOmics Ltd; PSA is employed by SimOmics Ltd; all other authors

475   declare no conflict of interest.

476

477   **Author Contributions**

478   DM, PSA, JT, LB and PMK designed the simulation model. DM implemented the

479   simulation model. LB and PMK designed the experimental study. DM, JWM, LB and

480   AS performed experimental studies. SH provided data and input on model

481   development. PSA and ATS designed and implemented the algorithm for the

482   generation of the artificial sinusoid structures. DM, LB, PSA, JT and PMK analyzed

483   the data and wrote the manuscript.

References

484

485

486   1.   Isaacs A, Lindenmann J. Virus interference. I. The interferon. Proc R Soc

487 Lond B Biol Sci. 1957;147(927):258-67. Epub 1957/09/12. PubMed PMID:

488 13465720.

489   2.   Isaacs A, Lindenmann J, Valentine RC. Virus interference. II. Some properties

490 of interferon. Proc R Soc Lond B Biol Sci. 1957;147(927):268-73. Epub 1957/09/12.

491 PubMed PMID: 13465721.

492   3.   Mackaness GB. The influence of immunologically committed lymphoid cells

493 on macrophage activity in vivo. J Exp Med. 1969;129(5):973-92. Epub 1969/05/01.

494 PubMed PMID: 4976110; PubMed Central PMCID: PMCPMC2138649.

495   4.   Chu T, Tyznik AJ, Roepke S, Berkley AM, Woodward-Davis A, Pattacini L,

496 et al. Bystander-activated memory CD8 T cells control early pathogen load in an

497 innate-like, NKG2D-dependent manner. Cell Rep. 2013;3(3):701-8. Epub

498 2013/03/26. doi: 10.1016/j.celrep.2013.02.020. PubMed PMID: 23523350; PubMed

499 Central PMCID: PMCPMC3628815.

500   5.   Griffith JW, Sokol CL, Luster AD. Chemokines and chemokine receptors:

501 positioning cells for host defense and immunity. Annu Rev Immunol. 2014;32:659-

502 702. Epub 2014/03/25. doi: 10.1146/annurev-immunol-032713-120145. PubMed

503 PMID: 24655300.

504   6.   Lertmemongkolchai G, Cai G, Hunter CA, Bancroft GJ. Bystander activation

505 of CD8+ T cells contributes to the rapid production of IFN-gamma in response to

506 bacterial pathogens. J Immunol. 2001;166(2):1097-105. Epub 2001/01/06. PubMed

507 PMID: 11145690.

508   7.   Mantovani A, Sica A, Sozzani S, Allavena P, Vecchi A, Locati M. The

509 chemokine system in diverse forms of macrophage activation and polarization. Trends

510 Immunol. 2004;25(12):677-86. Epub 2004/11/09. doi: 10.1016/j.it.2004.09.015.

511 PubMed PMID: 15530839.

512 8.   Polley R, Sanos SL, Prickett S, Haque A, Kaye PM. Chronic Leishmania

513 donovani infection promotes bystander CD8+-T-cell expansion and heterologous

514 immunity. Infect Immun. 2005;73(12):7996-8001. Epub 2005/11/22. doi:

515 10.1128/IAI.73.12.7996-8001.2005. PubMed PMID: 16299292; PubMed Central

516 PMCID: PMCPMC1307086.

517 9.   Tough DF, Borrow P, Sprent J. Induction of bystander T cell proliferation by

518 viruses and type I interferon in vivo. Science. 1996;272(5270):1947-50. Epub

519 1996/06/28. PubMed PMID: 8658169.

520 10.   Graham AL, Allen JE, Read AF. Evolutionary causes and consequences of

521 immunopathology. Annual review of Ecology, Evolution and Systematics.

522 2005;36:373-97. doi: 10.1146/annurev.ecolsys.36.102003.152622.

523 11.   Mills KH. Regulatory T cells: friend or foe in immunity to infection? Nat Rev

524 Immunol. 2004;4(11):841-55. Epub 2004/11/02. doi: 10.1038/nri1485. PubMed

525 PMID: 15516964.

526 12.   Sorci G, Cornet S, Faivre B. Immune evasion, immunopathology and the

527 regulation of the immune system. Pathogens. 2013;2(1):71-91. Epub 2013/01/01. doi:

528 10.3390/pathogens2010071. PubMed PMID: 25436882; PubMed Central PMCID:

529 PMCPMC4235712.

530 13.   Dorhoi A, Kaufmann SH. Perspectives on host adaptation in response to

531 Mycobacterium tuberculosis: modulation of inflammation. Semin Immunol.

532 2014;26(6):533-42. Epub 2014/12/03. doi: 10.1016/j.smim.2014.10.002. PubMed

533 PMID: 25453228.

534   14.   Pagan AJ, Ramakrishnan L. Immunity and Immunopathology in the

535   Tuberculous Granuloma. Cold Spring Harbor perspectives in medicine. 2015;5(9).

536   doi: doi: 10.1101/cshperspect.a018499. .

537   15.   Hams E, Aviello G, Fallon PG. The schistosoma granuloma: friend or foe?

538   Front Immunol. 2013;4:89. Epub 2013/04/19. doi: 10.3389/fimmu.2013.00089.

539   PubMed PMID: 23596444; PubMed Central PMCID: PMCPMC3625856.

540   16.   Kaye PM, Beattie L. Lessons from other diseases: granulomatous

541   inflammation in leishmaniasis. Semin Immunopathol. 2016;38(2):249-60. Epub

542   2015/12/19. doi: 10.1007/s00281-015-0548-7. PubMed PMID: 26678994; PubMed

543   Central PMCID: PMCPMC4779128.

544   17.   Lundy SK, Lukacs NW. Chronic schistosome infection leads to modulation of

545   granuloma formation and systemic immune suppression. Front Immunol. 2013;4:39.

546   Epub 2013/02/23. doi: 10.3389/fimmu.2013.00039. PubMed PMID: 23429492;

547   PubMed Central PMCID: PMCPMC3576626.

548   18.   Maroof A, Beattie L, Zubairi S, Svensson M, Stager S, Kaye PM.

549   Posttranscriptional regulation of Il10 gene expression allows natural killer cells to

550   express immunoregulatory function. Immunity. 2008;29(2):295-305. Epub

551   2008/08/15. doi: 10.1016/j.immuni.2008.06.012. PubMed PMID: 18701085; PubMed

552   Central PMCID: PMCPMC2656759.

553   19.   Mentink-Kane MM, Cheever AW, Thompson RW, Hari DM, Kabatereine

554   NB, Vennervald BJ, et al. IL-13 receptor alpha 2 down-modulates granulomatous

555   inflammation and prolongs host survival in schistosomiasis. Proc Natl Acad Sci U S

556   A. 2004;101(2):586-90. Epub 2003/12/31. doi: 10.1073/pnas.0305064101. PubMed

557   PMID: 14699044; PubMed Central PMCID: PMCPMC327191.

558   20.   Owens BM, Beattie L, Moore JW, Brown N, Mann JL, Dalton JE, et al. IL-10-

559   producing Th1 cells and disease progression are regulated by distinct CD11c(+) cell

560   populations during visceral leishmaniasis. PLoS Pathog. 2012;8(7):e1002827. Epub

561   2012/08/23. doi: 10.1371/journal.ppat.1002827. PubMed PMID: 22911108; PubMed

562   Central PMCID: PMCPMC3406093.

563   21.   Cotterell SE, Engwerda CR, Kaye PM. Leishmania donovani infection

564   initiates T cell-independent chemokine responses, which are subsequently amplified

565   in a T cell-dependent manner. Eur J Immunol. 1999;29(1):203-14. Epub 1999/02/05.

566   doi: 10.1002/(SICI)1521-4141(199901)29:01<203::AID-

567   IMMU203>3.0.CO;2-B. PubMed PMID: 9933102.

568   22.   Beattie L, Svensson M, Bune A, Brown N, Maroof A, Zubairi S, et al.

569   Leishmania donovani-induced expression of signal regulatory protein alpha on

570   Kupffer cells enhances hepatic invariant NKT-cell activation. Eur J Immunol.

571   2010;40(1):117-23. Epub 2009/10/31. doi: 10.1002/eji.200939863. PubMed PMID:

572   19877019; PubMed Central PMCID: PMCPMC2909397.

573   23.   Gupta G, Bhattacharjee S, Bhattacharyya S, Bhattacharya P, Adhikari A,

574   Mukherjee A, et al. CXC chemokine-mediated protection against visceral

575   leishmaniasis: involvement of the proinflammatory response. J Infect Dis.

576   2009;200(8):1300-10. Epub 2009/09/12. doi: 10.1086/605895. PubMed PMID:

577   19743920.

578   24.   Sato T, Thorlacius H, Johnston B, Staton TL, Xiang W, Littman DR, et al.

579   Role for CXCR6 in recruitment of activated CD8+ lymphocytes to inflamed liver. J

580   Immunol. 2005;174(1):277-83. Epub 2004/12/22. PubMed PMID: 15611250.

581   25.   Lee WY, Moriarty TJ, Wong CH, Zhou H, Strieter RM, van Rooijen N, et al.

582   An intravascular immune response to Borrelia burgdorferi involves Kupffer cells and

583 iNKT cells. Nat Immunol. 2010;11(4):295-302. Epub 2010/03/17. doi:

584 10.1038/ni.1855. PubMed PMID: 20228796; PubMed Central PMCID:

585 PMCPMC5114121.

586 26.   Wehr A, Baeck C, Heymann F, Niemietz PM, Hammerich L, Martin C, et al.

587 Chemokine receptor CXCR6-dependent hepatic NK T Cell accumulation promotes

588 inflammation and liver fibrosis. J Immunol. 2013;190(10):5226-36. Epub 2013/04/19.

589 doi: 10.4049/jimmunol.1202909. PubMed PMID: 23596313.

590 27.   Murray HW. Tissue granuloma structure-function in experimental visceral

591 leishmaniasis. Int J Exp Pathol. 2001;82(5):249-67. Epub 2001/11/13. PubMed

592 PMID: 11703536; PubMed Central PMCID: PMCPMC2517779.

593 28.   Muzumdar MD, Tasic B, Miyamichi K, Li L, Luo L. A global double-

594 fluorescent Cre reporter mouse. Genesis. 2007;45(9):593-605. Epub 2007/09/18. doi:

595 10.1002/dvg.20335. PubMed PMID: 17868096.

596 29.   Clausen BE, Burkhardt C, Reith W, Renkawitz R, Forster I. Conditional gene

597 targeting in macrophages and granulocytes using LysMcre mice. Transgenic Res.

598 1999;8(4):265-77. Epub 2000/01/06. PubMed PMID: 10621974.

599 30.   Beattie L, Peltan A, Maroof A, Kirby A, Brown N, Coles M, et al. Dynamic

600 imaging of experimental Leishmania donovani-induced hepatic granulomas detects

601 Kupffer cell-restricted antigen presentation to antigen-specific CD8 T cells. PLoS

602 Pathog. 2010;6(3):e1000805. Epub 2010/03/20. doi: 10.1371/journal.ppat.1000805.

603 PubMed PMID: 20300603; PubMed Central PMCID: PMCPMC2837408.

604 31.   Beattie L, d'El-Rei Hermida M, Moore JW, Maroof A, Brown N, Lagos D, et

605 al. A transcriptomic network identified in uninfected macrophages responding to

606 inflammation controls intracellular pathogen survival. Cell Host Microbe.

607   2013;14(3):357-68. Epub 2013/09/17. doi: 10.1016/j.chom.2013.08.004. PubMed

608   PMID: 24034621; PubMed Central PMCID: PMCPMC4180915.

609   32.   Alden K, Read M, Timmis J, Andrews PS, Veiga-Fernandes H, Coles M.

610   Spartan: a comprehensive tool for understanding uncertainty in simulations of

611   biological systems. PLoS Comput Biol. 2013;9(2):e1002916. Epub 2013/03/08. doi:

612   10.1371/journal.pcbi.1002916. PubMed PMID: 23468606; PubMed Central PMCID:

613   PMCPMC3585389.

614   33.   Svensson M, Zubairi S, Maroof A, Kazi F, Taniguchi M, Kaye PM. Invariant

615   NKT cells are essential for the regulation of hepatic CXCL10 gene expression during

616   Leishmania donovani infection. Infect Immun. 2005;73(11):7541-7. Epub

617   2005/10/22. doi: 10.1128/IAI.73.11.7541-7547.2005. PubMed PMID: 16239557;

618   PubMed Central PMCID: PMCPMC1273891.

619   34.   Fan J, Heller NM, Gorospe M, Atasoy U, Stellato C. The role of post-

620   transcriptional regulation in chemokine gene expression in inflammation and allergy.

621   Eur Respir J. 2005;26(5):933-47. Epub 2005/11/03. doi:

622   10.1183/09031936.05.00120204. PubMed PMID: 16264057.

623   35.   An G. Concepts for developing a collaborative in silico model of the acute

624   inflammatory response using agent-based modeling. J Crit Care. 2006;21(1):105-10;

625   discussion 10-1. Epub 2006/04/18. doi: 10.1016/j.jcrc.2005.11.012. PubMed PMID:

626   16616634.

627   36.   An G, Christley S. Addressing the translational dilemma: dynamic knowledge

628   representation of inflammation using agent-based modeling. Crit Rev Biomed Eng.

629   2012;40(4):323-40. Epub 2012/11/13. PubMed PMID: 23140123.

630   37.   Moore JW, Moyo D, Beattie L, Andrews PS, Timmis J, Kaye PM. Functional

631   complexity of the Leishmania granuloma and the potential of in silico modeling.

632 Front Immunol. 2013;4:35. Epub 2013/02/21. doi: 10.3389/fimmu.2013.00035.

633 PubMed PMID: 23423646; PubMed Central PMCID: PMCPMC3573688.

634 38. Hoehme S, Brulport M, Bauer A, Bedawy E, Schormann W, Hermes M, et al.

635 Prediction and validation of cell alignment along microvessels as order principle to

636 restore tissue architecture in liver regeneration. Proc Natl Acad Sci U S A.

637 2010;107(23):10371-6. Epub 2010/05/21. doi: 10.1073/pnas.0909374107. PubMed

638 PMID: 20484673; PubMed Central PMCID: PMCPMC2890786.

639 39. Wambaugh J, Shah I. Simulating microdosimetry in a virtual hepatic lobule.

640 PLoS Comput Biol. 2010;6(4):e1000756. Epub 2010/04/28. doi:

641 10.1371/journal.pcbi.1000756. PubMed PMID: 20421935; PubMed Central PMCID:

642 PMCPMC2858695.

643 40. Egen JG, Rothfuchs AG, Feng CG, Winter N, Sher A, Germain RN.

644 Macrophage and T cell dynamics during the development and disintegration of

645 mycobacterial granulomas. Immunity. 2008;28(2):271-84. Epub 2008/02/12. doi:

646 10.1016/j.immuni.2007.12.010. PubMed PMID: 18261937; PubMed Central PMCID:

647 PMCPMC2390753.

648 41. Bouwens L, Baekeland M, De Zanger R, Wisse E. Quantitation, tissue

649 distribution and proliferation kinetics of Kupffer cells in normal rat liver. Hepatology.

650 1986;6(4):718-22. Epub 1986/07/01. PubMed PMID: 3733004.

651 42. Sleyster EC, Knook DL. Relation between localization and function of rat

652 liver Kupffer cells. Lab Invest. 1982;47(5):484-90. Epub 1982/11/01. PubMed PMID:

653 6182391.

654 43. Geissmann F, Cameron TO, Sidobre S, Manlongat N, Kronenberg M, Briskin

655 MJ, et al. Intravascular immune surveillance by CXCR6+ NKT cells patrolling liver

656 sinusoids. PLoS Biol. 2005;3(4):e113. Epub 2005/04/01. doi:

657   10.1371/journal.pbio.0030113. PubMed PMID: 15799695; PubMed Central PMCID:

658   PMCPMC1073691.

659   44.   Weber M, Hauschild R, Schwarz J, Moussion C, de Vries I, Legler DF, et al.

660   Interstitial dendritic cell guidance by haptotactic chemokine gradients. Science.

661   2013;339(6117):328-32. Epub 2013/01/19. doi: 10.1126/science.1228456. PubMed

662   PMID: 23329049.

663   45.   Matsuda JL, Gapin L, Sidobre S, Kieper WC, Tan JT, Ceredig R, et al.

664   Homeostasis of V alpha 14i NKT cells. Nat Immunol. 2002;3(10):966-74. Epub

665   2002/09/24. doi: 10.1038/ni837. PubMed PMID: 12244311.

666   46.   Davis JM, Ramakrishnan L. The role of the granuloma in expansion and

667   dissemination of early tuberculous infection. Cell. 2009;136(1):37-49. Epub

668   2009/01/13. doi: 10.1016/j.cell.2008.11.014. PubMed PMID: 19135887; PubMed

669   Central PMCID: PMCPMC3134310.

670   47.   Egen JG, Rothfuchs AG, Feng CG, Horwitz MA, Sher A, Germain RN.

671   Intravital imaging reveals limited antigen presentation and T cell effector function in

672   mycobacterial granulomas. Immunity. 2011;34(5):807-19. Epub 2011/05/21. doi:

673   10.1016/j.immuni.2011.03.022. PubMed PMID: 21596592; PubMed Central PMCID:

674   PMCPMC3164316.

675   48.   Flugge AJ, Timmis J, Andrews PS, Moore JW, Kaye PM. Modelling and

676   simulation of granuloma formation in visceral leishmaniasis. Evolutionary

677   Computation, 2009 CEC '09; IEEE Congress 20092009. p. 3052 - 9.

678   49.   Beattie L, Sawtell A, Mann J, Frame TC, Teal B, de Labastida Rivera F, et al.

679   Bone marrow-derived and resident liver macrophages display unique transcriptomic

680   signatures but similar biological functions. J Hepatol. 2016;65(4):758-68. Epub

681 2016/06/06. doi: 10.1016/j.jhep.2016.05.037. PubMed PMID: 27262757; PubMed

682 Central PMCID: PMCPMC5028381.

683 50.   Amprey JL, Im JS, Turco SJ, Murray HW, Illarionov PA, Besra GS, et al. A

684 subset of liver NK T cells is activated during Leishmania donovani infection by

685 CD1d-bound lipophosphoglycan. J Exp Med. 2004;200(7):895-904. Epub

686 2004/10/07. doi: 10.1084/jem.20040704. PubMed PMID: 15466622; PubMed Central

687 PMCID: PMCPMC2213292.

688 51.   Robert-Gangneux F, Drogoul AS, Rostan O, Piquet-Pellorce C, Cayon J,

689 Lisbonne M, et al. Invariant NKT cells drive hepatic cytokinic microenvironment

690 favoring efficient granuloma formation and early control of Leishmania donovani

691 infection. PLoS One. 2012;7(3):e33413. Epub 2012/03/30. doi:

692 10.1371/journal.pone.0033413. PubMed PMID: 22457760; PubMed Central PMCID:

693 PMCPMC3310876.

694 52.   Gasteiger G, Fan X, Dikiy S, Lee SY, Rudensky AY. Tissue residency of

695 innate lymphoid cells in lymphoid and nonlymphoid organs. Science.

696 2015;350(6263):981-5. Epub 2015/10/17. doi: 10.1126/science.aac9593. PubMed

697 PMID: 26472762; PubMed Central PMCID: PMCPMC4720139.

698 53.   Robinette ML, Fuchs A, Cortez VS, Lee JS, Wang Y, Durum SK, et al.

699 Transcriptional programs define molecular characteristics of innate lymphoid cell

700 classes and subsets. Nat Immunol. 2015;16(3):306-17. Epub 2015/01/27. doi:

701 10.1038/ni.3094. PubMed PMID: 25621825; PubMed Central PMCID:

702 PMCPMC4372143.

703 54.   Juno JA, Keynan Y, Fowke KR. Invariant NKT cells: regulation and function

704 during viral infection. PLoS Pathog. 2012;8(8):e1002838. Epub 2012/08/24. doi:

705   10.1371/journal.ppat.1002838. PubMed PMID: 22916008; PubMed Central PMCID:

706   PMCPMC3420949.

707   55.   Mattarollo SR, West AC, Steegh K, Duret H, Paget C, Martin B, et al. NKT

708   cell adjuvant-based tumor vaccine for treatment of myc oncogene-driven mouse B-

709   cell lymphoma. Blood. 2012;120(15):3019-29. Epub 2012/08/31. doi: 10.1182/blood-

710   2012-04-426643. PubMed PMID: 22932803; PubMed Central PMCID:

711   PMCPMC3557399.

712   56.   Mussai F, De Santo C, Cerundolo V. Interaction between invariant NKT cells

713   and myeloid-derived suppressor cells in cancer patients: evidence and therapeutic

714   opportunities. J Immunother. 2012;35(6):449-59. Epub 2012/06/28. doi:

715   10.1097/CJI.0b013e31825be926. PubMed PMID: 22735803.

716   57.   Pilones KA, Aryankalayil J, Demaria S. Invariant NKT cells as novel targets

717   for immunotherapy in solid tumors. Clin Dev Immunol. 2012;2012:720803. Epub

718   2012/11/03. doi: 10.1155/2012/720803. PubMed PMID: 23118781; PubMed Central

719   PMCID: PMCPMC3483734.

720   58.   Gonzalez-Aseguinolaza G, de Oliveira C, Tomaska M, Hong S, Bruna-

721   Romero O, Nakayama T, et al. alpha -galactosylceramide-activated Valpha 14 natural

722   killer T cells mediate protection against murine malaria. Proc Natl Acad Sci U S A.

723   2000;97(15):8461-6. Epub 2000/07/19. PubMed PMID: 10900007; PubMed Central

724   PMCID: PMCPMC26970.

725   59.   Chackerian A, Alt J, Perera V, Behar SM. Activation of NKT cells protects

726   mice from tuberculosis. Infect Immun. 2002;70(11):6302-9. Epub 2002/10/16.

727   PubMed PMID: 12379709; PubMed Central PMCID: PMCPMC130331.

728   60.   Albergante L, Timmis J, Beattie L, Kaye PM. A Petri net model of

729   granulomatous inflammation: implications for IL-10 mediated control of Leishmania

730 donovani infection. PLoS Comput Biol. 2013;9(11):e1003334. Epub 2013/12/24. doi:

731 10.1371/journal.pcbi.1003334. PubMed PMID: 24363630; PubMed Central PMCID:

732 PMCPMC3867212.

733

Figure Legends

735   **Figure 1.** *L. donovani* **infection induces transactivation of Kupffer cells for**

736   **chemokine production**

737   (**A**) Heat map showing chemokine mRNA abundance in flow sorted Kupffer cells

738   from naïve mice (control) and from KCs isolated from infected mice and separated

739   into those containing parasites ("infected") and those that do not contain parasites

740   ("inflamed"). KC isolation was performed at 2h and 12h post infection, with matched

741   controls. Lanes numbered 1-4 indicates separate sorts. The gating strategy for

742   separating "infected" from "inflamed" KCs is provided in Figure 3 of reference 31. (**B**

743   and **C**) Two modeling scenarios were generated. In scenario 1 (panel B), only

744   infected KCs produce sufficient chemokine to attract and retain NKT cells. In

745   scenario 2 (panel C) both infected and inflamed KCs produce chemokines to attract

746   NKT cells, although only infected KCs have the ability to retain these through

747   cognate interactions.

748

749   **Figure 2. Overview of the liver agent based model**

750   (**A**) A simulated sinusoidal network was constructed in quasi-2D space using a

751   sinusoidal structure generation algorithm (see **Supplemental Experimental**

752   **Procedures**). A drain node representing the portal vein (black) is placed in the centre

753   of a 2D space with six surrounding entry nodes representing the portal triads (green),

754   forming an irregular hexagon layout (i). Sinusoids (red) are grown from entry nodes

755   to the drain node (ii). Additional entry nodes created around original entry nodes

756   conceptual form a portal triad (iii), allow additional sinusoids to be grown (iv).

757   Additional sinusoid branches are added between existing sinusoids (v).

758   Execution of the algorithm is shown in **Movie S1.** (**B**) Node structure of the model

759   underlying KC placement and chemokine diffusion. Nodes are populated or not with

760   a single KC, and may attract NKT cells to that node. Chemokines exert their effect

761   by "diffusing" across nodes. For further details, see text and **Supplementary**

762   **Experimental Procedures**. (**C**) Snapshot of 2-photon image of liver from (mT/mG x

763   lysMcre)$_{F1}$ mice, showing sinusoids (red) and KCs (green).

764

765   **Figure 3. Response landscapes for parasite-induced KC activation with and**
766   **without KC activation in trans.**
767
768   (**A-D**) Two-at-a-time (TAT) parameter analysis showing the effect on total KC

769   stimulation time (A, C) and on % inflammatory foci (B and D) of modifying either

770   cumulative time to activate KCs and parasite-induced activation time (A and B)

771   or cumulative time to activate KCs and bystander activation time (C and D). For

772   further details, see **Supplementary Experimental Procedures**.

773

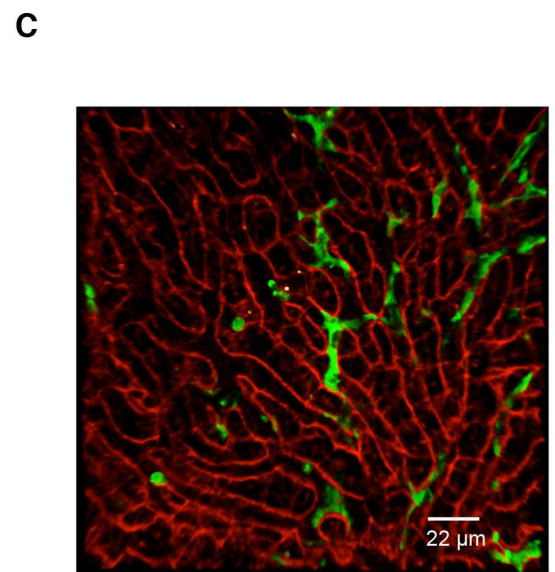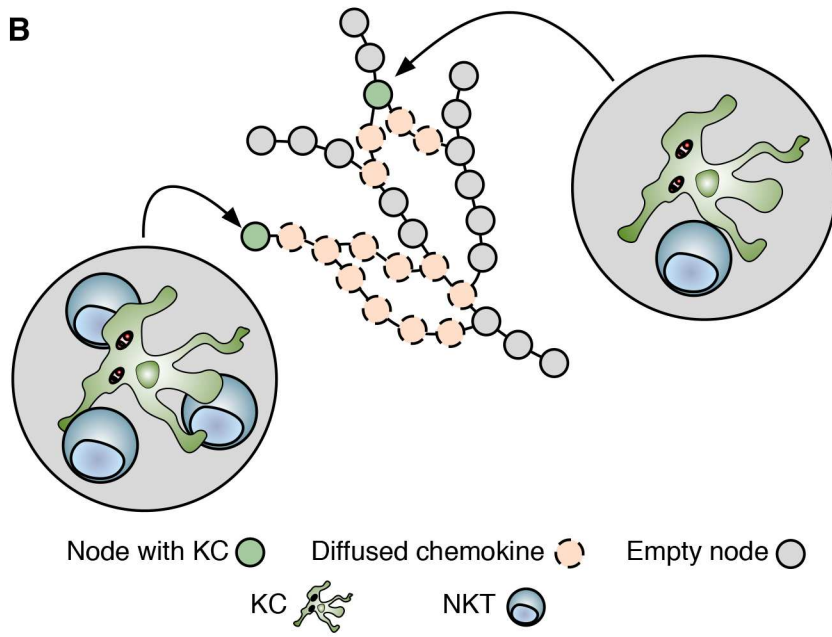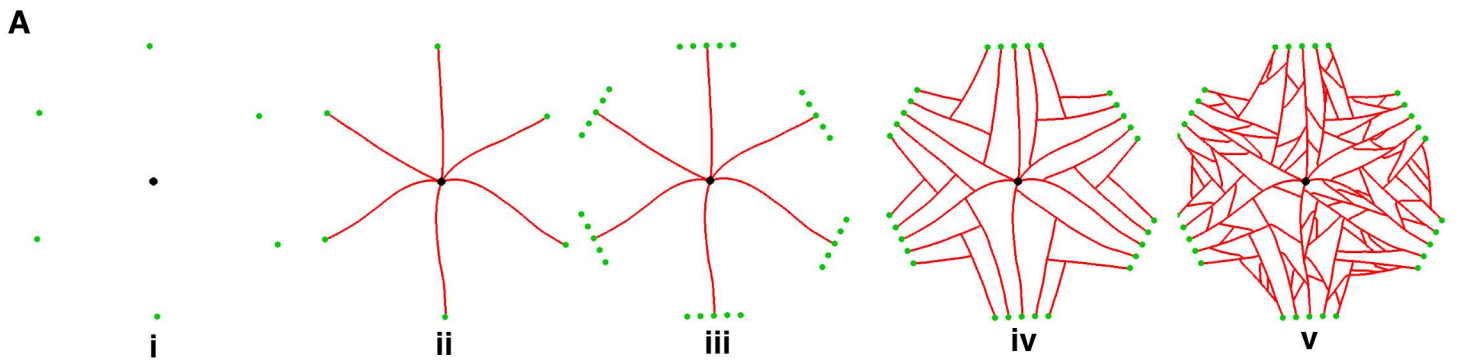774   **Figure 4. Expansion of NKT Cells promotes granuloma formation**

775   (**A**) Alternate hypotheses for impact of increasing NKT cell number. (**B**) Increasing

776   NKT cells in silico leads to greater percentages of KCs that form an inflammatory

777   focus, when qualified at 4, 6 and 8 cells. (**C - E**) Absolute numbers of NKT (C), NK

778   (D) and T cells (E) in naïve and infected mice with or without administration of rIL-

779   15. Results are pooled from two independent experiments and represent mean±SEM

780   (n=10 mice per group). *P<0.05, **P<0.01, ***P<0.001, by paired Students t-test.

781   (**F**) Percentage of infected KCs with surrounding granuloma in control and rIL-15-

782   treated infected mice. **P<0.01 (n=10 mice). (**G** and **H**) Heterogeneity of

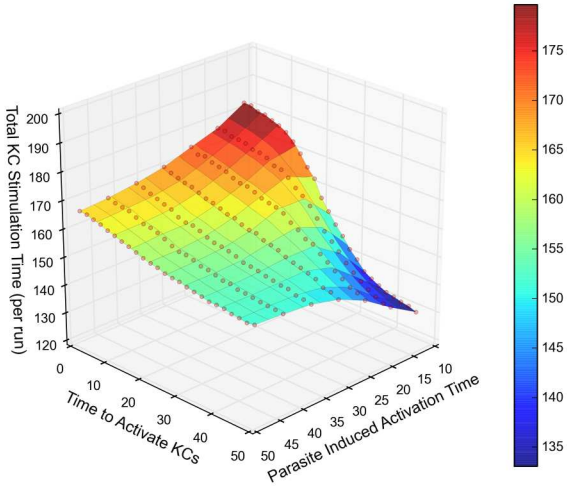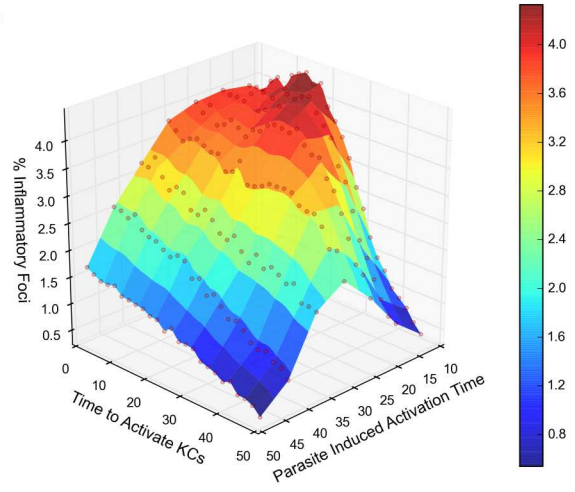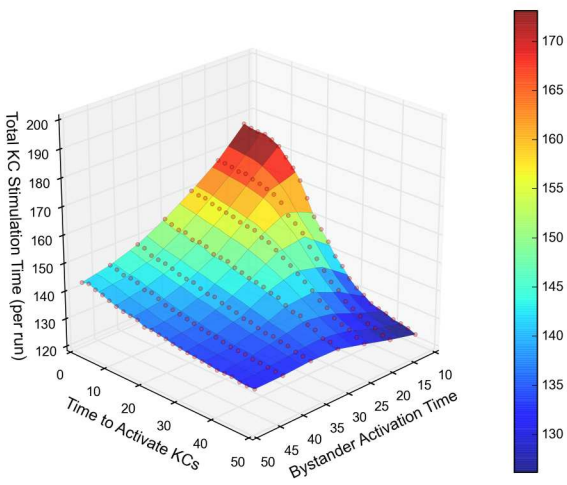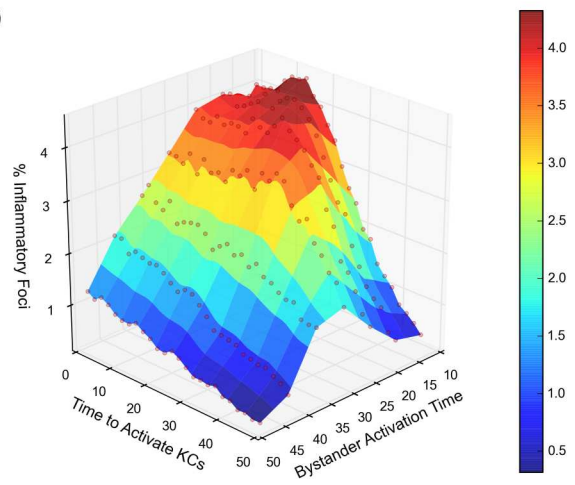783   granulomas comparing infected (G) and rIL-15-treated (H) mice infected with

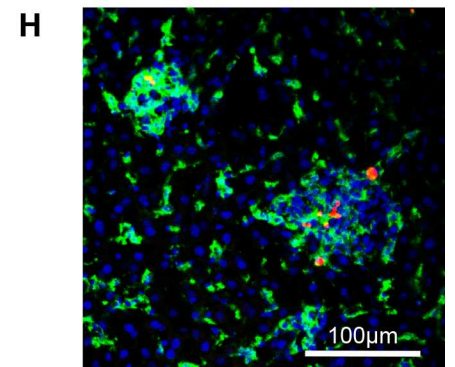784   TdTomato-*L. donovani* (red). Sections were stained using F4/80 (green) and
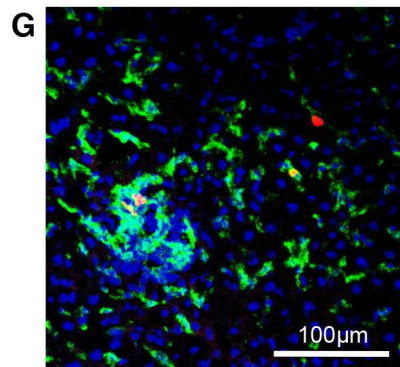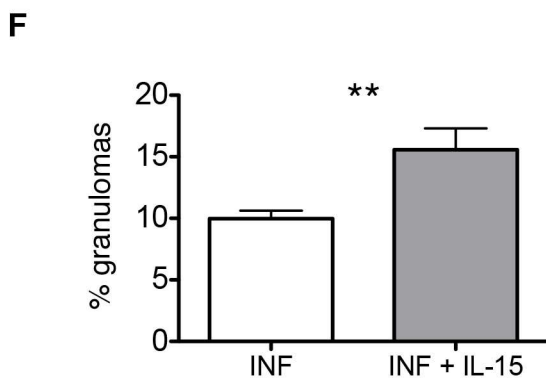
785   counterstained with DAPI (blue).

786

A

i ii iii iv v

B

Node with KC 🟢   Diffused chemokine 🔶   Empty node ⚪

KC 🦠   NKT 🔵

C

22 μm

A

B

Parasite Induced Activation + Bystander Activation

% Inflammatory Foci

base   2-fold   3-fold

■ % Foci > 4 Cells   ■ % Foci > 6 Cells   ■ % Foci > 8 Cells

C

NKT cells

Absolute cell number

ns

***

**

naive   IL-15   INF   INF+IL-15

D

NK cells

Absolute cell number

*

***

ns

naive   IL-15   INF   INF+IL-15

E

T cells

Absolute cell number

*

***

ns

naive   IL-15   INF   INF+IL-15

F

% granulomas

**

INF   INF + IL-15

G

100μm

H

100μm

Supplemental Information

Macrophage transactivation for chemokine production negatively regulates granulomatous inflammation.

Daniel Moyo[1,2], Lynette Beattie[1*], Paul S Andrews[3], John W J Moore[1], Jon Timmis[3], Amy Sawtell[1], Stefan Hoehme[4], Adam T. Sampson[5], Paul M Kaye[1]

Supplemental Figures

Figure S1. Related to Figure 2. Generation of Nodes and Edges of a Sinusoid Network.
(A-D) See Algorithm 1 in Supplemental Experimental Procedures. (E) Effect on percentage inflammatory foci qualified at 4, 6 and 8 cells, when modifying maximum chemokine diffusion distance.

A

(A1)

aware

[δ(NKT)] (A5) → stimulated

Interrogate
local node
IFN-γ

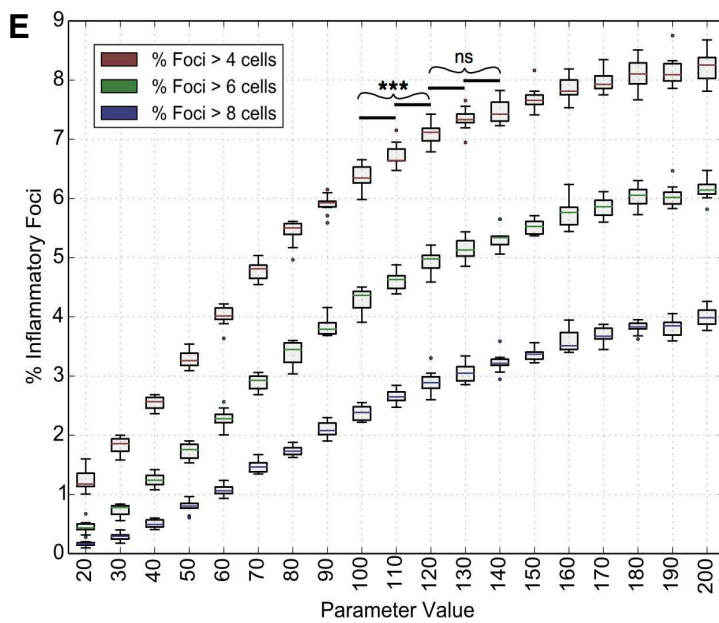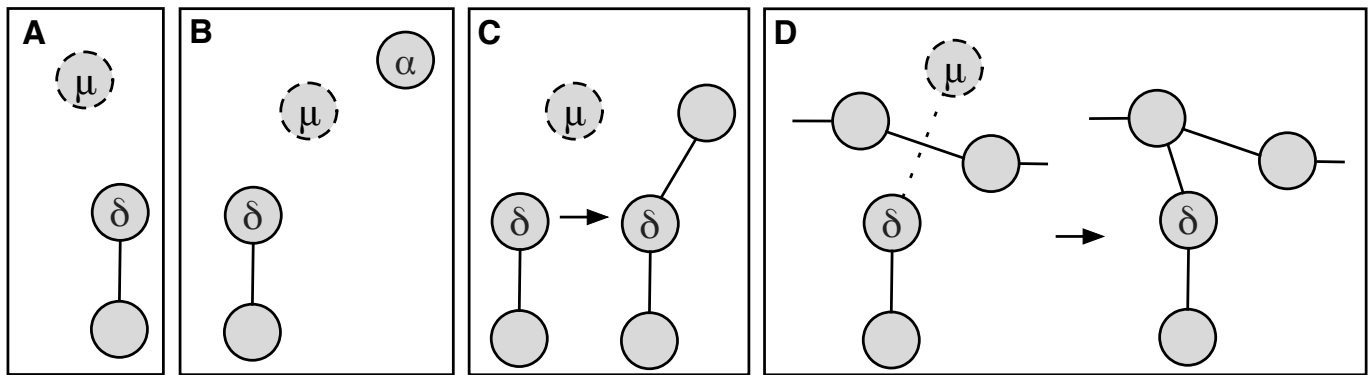[NO δ(NKT)] → diffuse basal level of
chemo-attractant

[IFN-γ > ifnThreshold]
(A7)

engaged

[δ(NKT)] → increment attraction
function
(A2,A6)

[δ(NKT)] → increment retention
function
(A2,A6)

B

aware

diffuse basal level of
attraction

C

ActionState

recovering

[t > (X ~ N(μ, σ2)] (A4) →

inactive

[co-located with infected KC] →

producing
(IFN-γ)

[co-located with
uninfected KC]

[δ(leave)]

MoveState

[co-located with uninfected KC]

in-blood
(reset cell
details)

(A3) →

patrolling
(A6)

[node attraction level > 0]
(A5) →

chemotaxing
(A1)

[co-located with infected KC]
(A2) →

aggregating
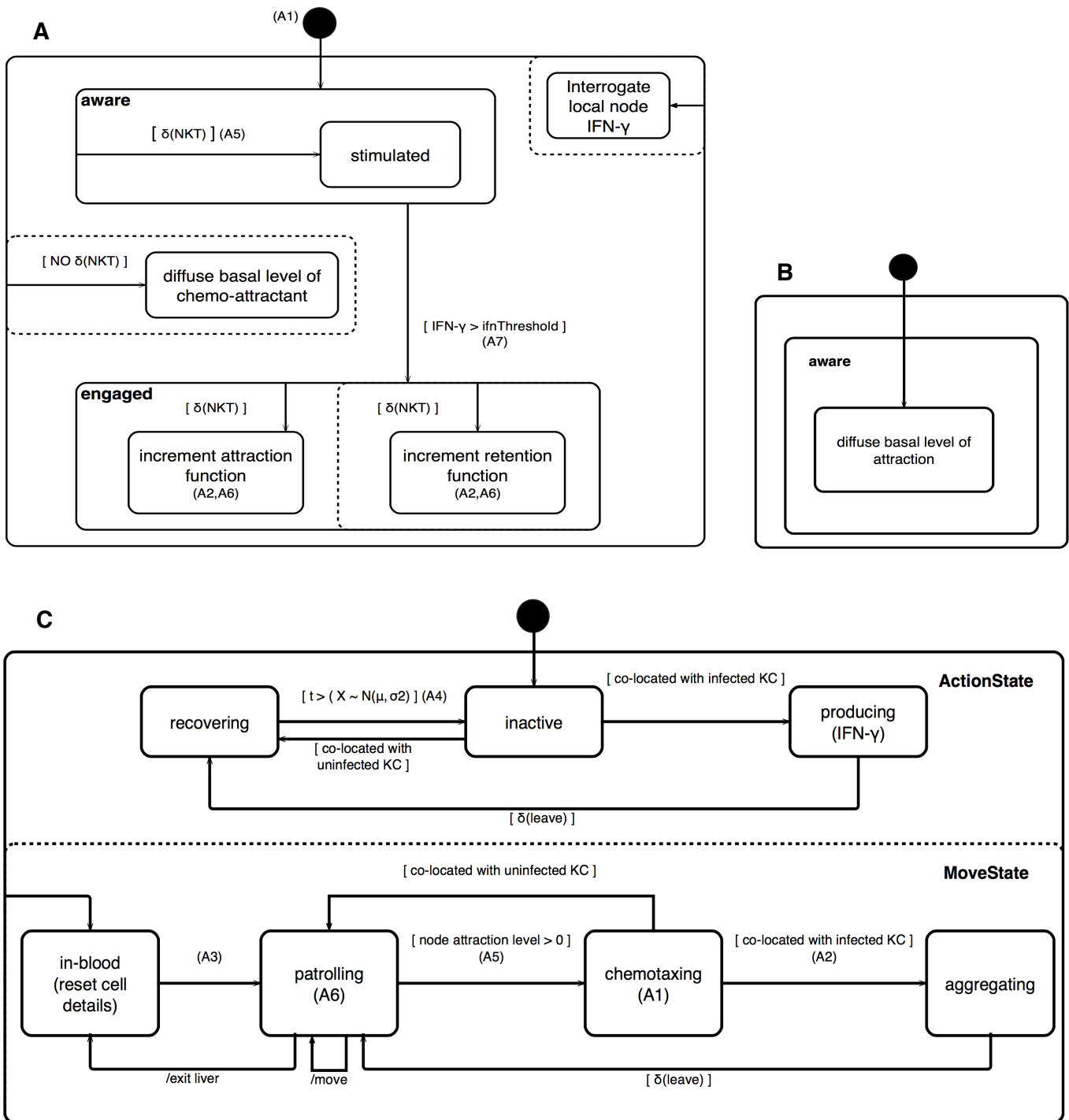
/exit liver   /move   [δ(leave)]

Figure S2. Related to Figure 2. State-diagrams for Kupffer cell and NKT cell behaviors.
(A) Infected Kupffer Cell; (B) uninfected Kupffer Cell; (C) NKT cell. See State Transition Diagrams in Supplemental Experimental Procedures.
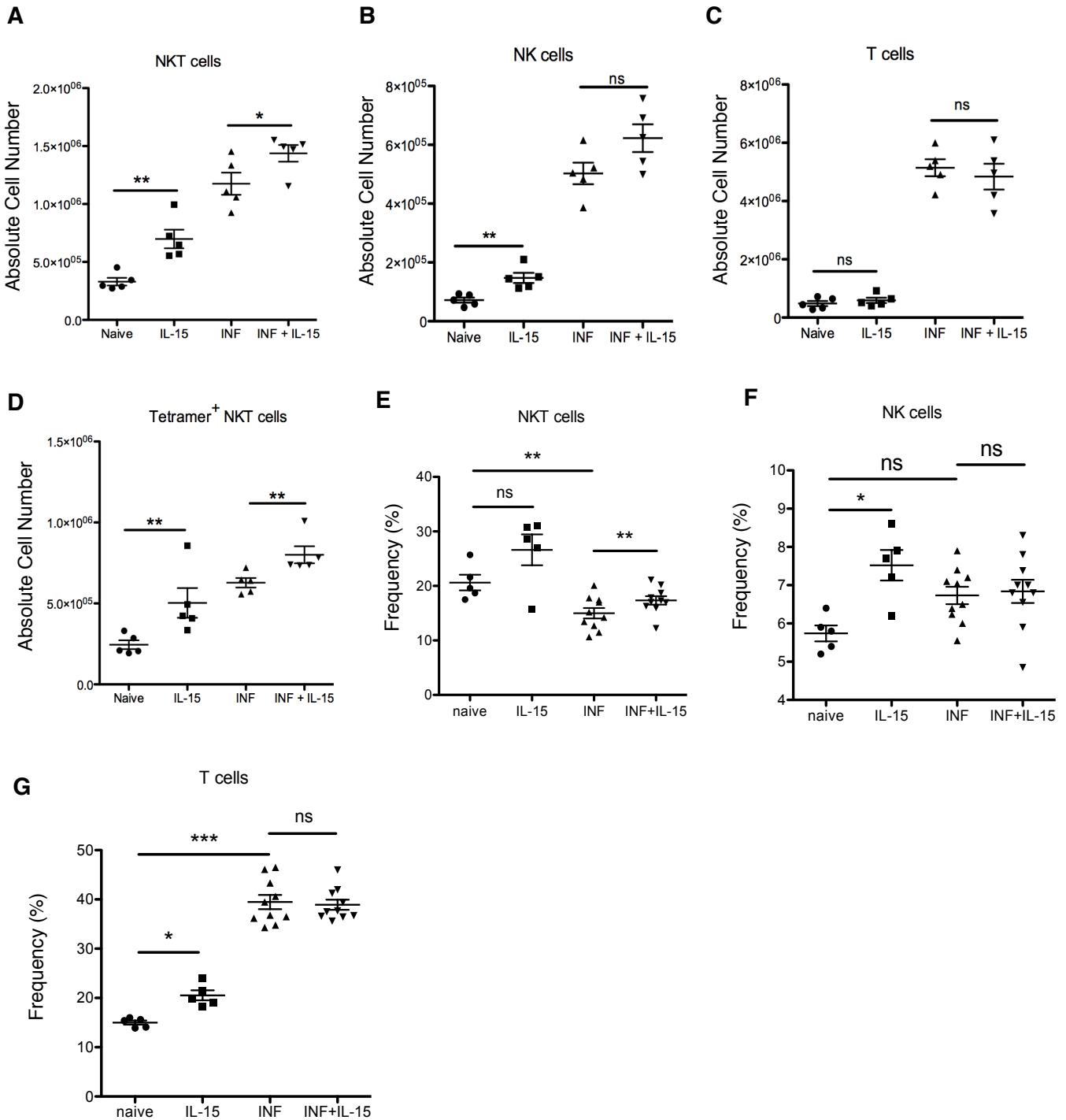
Figure S3. Related to Figure 4. IL-15 Promotes NKT Cell Expansion.
(A) Absolute cell numbers for NKT, (B) NK and (C) T cells, and (D) CD1d tetramer+ NKT cells for naïve, IL-15 treated naïve (IL-15), infected (INF) and IL-15 pre-treated infected (INF+IL-15) mice. (E) Relative frequency of NKT, (F) NK and (G) T cells for naïve, IL-15 treated naïve (IL-15), infected (INF) and IL-15 pre-treated infected (INF+IL-15) mice. Results are depicted as mean ± SEM of 5 mice per group. *P≤0.05, **P≤0.01 paired Students t-test.

Figure S4. Related to Figure 2. Aleatory Analysis Determines a Minimum of 300 Simulation Runs per Experiment.
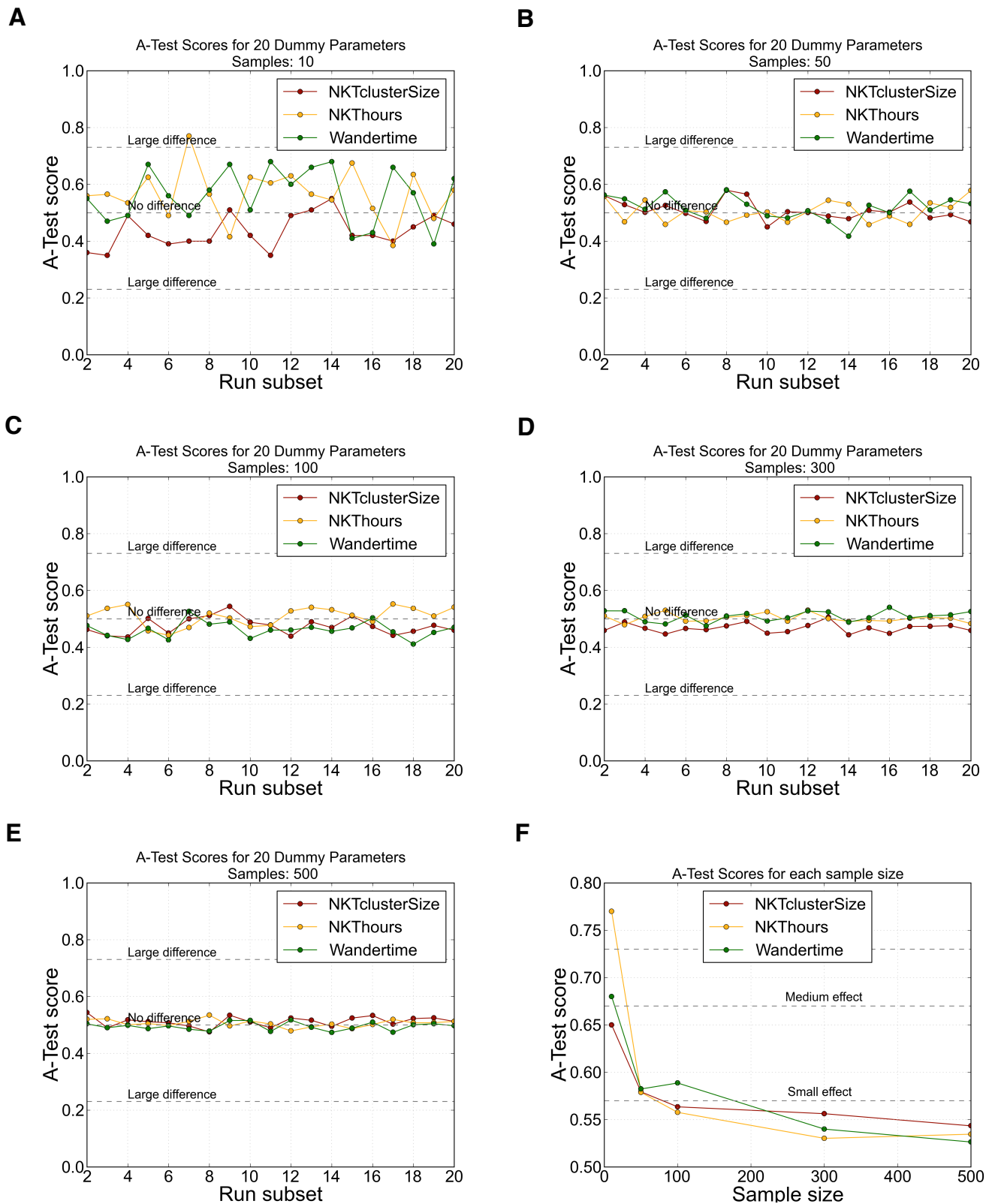A-test (Vargha and Delaney, 2000) scores for three simulation output measures across sample sizes of (A) 10, (B) 50, (C) 100, (D) 300 and (E) 500, illustrating that greater than 300 simulation runs are needed to capture the variation in output results and mitigate uncertainty, summarized in (F).

Supplemental Tables

Biological Parameters	Value	Source
NKT cell velocity in the sinusoids	10-20μm/minute	(Geissmann et al., 2005)
NKT cell numbers in a section of mouse liver lobule	$\sim$49($\sim$1:3 ratio with KCs)	Derived from (Lee et al., 2010) and unpublished data
Kupffer cell numbers per gram	14-20 x 10^6/g	(Bouwens et al., 1986)
Infected KCs at 2 hours	$\sim$23%	Unpublished data
KCs per lobule section	$\sim$146	Unpublished data
Non-branched segment length	43.1 $\pm$ 2.25 μm	(Höhme et al., 2010)
Mean branching angles of sinusoids	32.5° $\pm$ 11.2°	(Höhme et al., 2010)
KC spatial distribution	Percentages: Periportal (PP) - 43 Midzonal (MZ) - 28 Centrilobular (CV) - 29 Ratios: 4(PP), 3(MZ), 2(CV)	(Bouwens et al., 1986; Sleyster and Knook, 1982)

Table S1. Related to Figure 2. Table of biological parameters used for calibration.

	Domain	Platform	Justification
KC_A1		Infected KCs are infected at initiation of the simulation, t(0).	KCs rapidly phagocytose parasites. We are not investigating conditions pre-infection.
KC_A2		Infected KCs can recruit and retain cells.	Unpublished data.
KC_A3		Uninfected KCs can only recruit cells.	Unpublished data.
KC_A4	KCs are immobile	KCs have no movement rules	(Lee et al., 2010)
KC_A5	KC retention of NKT cells is probabilistic, mediated by SIRP-a - CD47 interactions and local IFN-g concentration.	Cognate interactions occur when two cells are co-located on the same node and are not modeled explicitly. Retention is modeled probabilistically using a function modified by local IFN-g level	(Beattie et al., 2010; Svensson et al., 2005)
KC_A6	NKT produced IFN-g affects KC attractive chemokine production.	Retentive chemokine level increases in-line with local IFN-g level and increases the diffusion distance of attractive chemokine linearly. Retentive chemokine diffusion distance can decay.	Simplification, no experimental data available.
KC_A7	There is a threshold level of stimulation required to activate a KC.	KCs will not transition to an engaged state until a threshold level of IFN-g is reached.	To facilitate implementation, no experimental data available.
NKT_A1	NKT cells respond to chemo- attractant	NKT cells under chemotaxis, when presented with two or more attraction gradients, will choose a direction based on attractive chemokine strength.	To facilitate implementation, no experimental data available.
NKT_A2	NKT cells interact with KCs	NKT cells will interact with the first infected KC they encounter whilst in chemotaxis.	To facilitate implementation, no experimental data available.
NKT_A3		The NKT cell population of the lobule section remains constant; cells exiting the environment will enter as new cells via an entry point.	
NKT_A4	NKT cells are capable of becoming anergic	NKT cells are refractive to stimulation and take a period of time to recover after stimulating and leaving a KC.	(Iyoda et al., 2010)
NKT_A5		NKT cells will respond immediately to a chemokine signal.	To facilitate implementation, no experimental data available.
NKT_A6	NKT cells can walk the sinusoids and switch direction probabilistically NKT cells perform a random walk of the tree- node structure, and a probability governs their	NKT cells perform a random walk of the tree-node structure, and a probability governs their ability to turn in the sinusoids at random.	(Geissmann et al., 2005)
C_A1	Attractive chemokines flow in the same direction as blood would.	Attraction diffuses downstream of infected KCs towards the central vein.	Chemotaxis in 3D environments is poorly understood (Haessler et al., 2011)
C_A2		Strength of attractive chemokine is a function of distance from source, calculated using a simplified Ficks Law of diffusion.	To facilitate implementation.
C_A3		Chemokine growth is calculated using a sigmoid function.	To facilitate implementation, no experimental data available.

Table S2. Related to Figure 2. Modelling Assumptions. Statement of assumptions made regarding the underlying biological domain (domain) and how we have abstracted this information in the engineered simulation (platform). Assumptions labeled KC_ relate to Kupffer Cells, NKT_ to NKT Cells, and C_ to chemokines. Assumptions make it possible to model when data is limited or there is a gap in understanding or the literature.

	Parameter	Value	Units	Description	Source
Simulation	p_numInfectedKCs	33	cells	Number of infected kupffer cells in a π*(284μm)^2 sectional area of sinusoid.	Calibrated to unpublished data
	p_numUninfected	113	cells	Number of uninfected kupffer cells in a π*(284μm)^2 sectional area of sinusoid.	
	p_numNKTs	49	cells	Number of NKT cells in a π*(284μm)^2 sectional area of sinusoid.	Calibrated to unpublished data and (Lee et al., 2010)·(Geissmann et al., 2005)
Chemokine	p_chemoAttract	43200	iterations	Stimulation time required to reach maximum attractive chemokine concentration.	No biological equivalent; explored and chosen through parameter sensitivity analysis
	p_chemoRetain	172800	iterations	Interaction time required to reach maximum retentive chemokine concentration.	
	p_chemoIFN	172800	iterations	Interaction time required to reach activate infected KCs.	

	Parameter	Value	Units	Description	Source
NKT cell	p_turnProb	0.005	probability	Probability that an NKT cell will reverse direction in the sinusoids.	No biological equivalent; explored and chosen through parameter sensitivity analysis.
	p_moveMin	3	iterations	Value given to link simulation iterations to NKT cell velocity.	Calibrated to published NKT cell speeds from (Geissmann et al., 2005)
	p_moveMax	6			
	p_anergicItns	3600	iterations	Time in iterations for an NKT cell to remain unable to stimulate a KC.	No biological equivalent; explored and chosen through parameter sensitivity analysis.
	p_escapeItns	600	iterations	Time in iterations for an NKT cell to escape the influence of KC produced chemo-attractant.	
	p_leaveProb	0.000265306	probability	The probability of an interacting NKT cell leaving the location of an infected KC.	
	p_minLeaveProb	0.00005	probability	To guard against the probabilistic tipping point whereby retention causes cells to never leave.	
	p_chemoIFN	172800	iterations	Interaction time required to reach maximum attractive chemokine concentration.	
Kupffer cell	p_chemoDist	20	distance(nodes)	Starting diffusion distance for attractive chemokine.	No biological equivalent; explored and chosen through parameter sensitivity analysis.
	p_ratioCV	0.1	percentage	Ratio of infected cells in the CV region of the lobule section	Bouwens et al., 1986. Sleyster et al., 1982.
	p_ratioMZ	0.25	percentage	Ratio of infected cells in the MZ region of the lobule section	
	p_ratioPP	0.65	percentage	Ratio of infected cells in the PP region of the lobule section	
	p_maxDist	200	distance(nodes)	Maximum diffusion distance for attractive chemokine.	Calibrated to twice reported max(Weber et al., 2013)
	p_ifnThreshold	0.999	threshold	Threshold value of IFN-γ required to activate a KC. Chemokine function f(x)→1, therefore a threshold is required.	No biological equivalent

Table S3. Related to Figure 2. Simulation Parameters. Summary of the simulation parameters, descriptions of their purpose, values and any data sources for parameters relating to cell numbers and chemokine functions. All estimated values are based on a comprehensive sensitivity analysis for parameters that have unknown or no clear biological value.

Supplemental Movies

Movie S1. Related to Figure2. Sinusoid structure generation algorithm. Execution of the sinusoid structure generation algorithm at 8x speed. Drain node (cyan), entry nodes (green) and sinusoids (red).

Supplemental Experimental Procedures

We assume that our sinusoid network exists in a quasi-2D space (we can consider this as a slice through a 3D lobule). We also assume that the lobule structure is roughly hexagonal with a single central vein in the centre and six portal triad areas placed at roughly regular intervals around the central vein. The flow of blood borne cells is assumed to be from portal triads to the central vein, so in the algorithmic description below the central vein is termed a drain node, and the portal triad regions deemed entry nodes.

Algorithm 1 describes how the nodes and edges of the sinusoid network are generated, whilst Algorithm 2 describes how the overall sinusoid network (the lobule) is generated using Algorithm 1. Höhme et al. (2010) provide us with the following statistics that guide Algorithm 2:

- Average length between central vein and portal triad = 284μm;

- Average length of a non-branched sinusoid = 43.1μm;

- Average angle between branching sinusoids = $32.5°$.

Algorithm 1: Sinusoid branch generation

1. A potential new node (μ) is generated 1μm from the current node (δ)

    (a) If we are within range of an attracting node (α) then μ is generated in the direction of α (see Figure S4(B)).

    (b) Otherwise μ is generated based on our current direction with a small random adjustment (see Figure S4(A)).

2. Create a new edge between δ and another node:

    (a) If the line between δ and μ intersects another edge in the sinusoid network, then connect δ to the closest existing node (see Figure S4(D)).

    (b) Otherwise connect δ and μ (see Figure S4(C)).

3. Repeat Steps 1 and 2 until an intersection is detected.

Algorithm 2: Sinusoid network (lobule) generation

1. A drain node (representing the central vein) is placed in the centre of the 2D space, surrounded by six entry nodes (representing the locations of portal triads) in an irregular hexagon formation (see Figure 2(Ai)). The exact location of the entry nodes is determined stochastically.

2. For each of the six entry nodes a sinusoid branch is grown (see algorithm 1) from the entry node towards the attracting drain node (see Figure 2(Aii)).

3. An additional set of entry nodes is created for each original entry node and aligned with the original node. These additional nodes represent additional sources of blood supply coming out of the portal triad (see Figure 2(Aiii)).

4. For each of the new entry nodes a sinusoid branch is grown (see algorithm 1) from the entry node towards the existing sinusoid structure (see Figure 2(Aiv)).

5. Additional sinusoids are created to connect existing sinusoids (see Figure 2(Av)).

    - Select the longest sinusoid in the structure
    - Select a node in the longest sinusoid and grow a sinusoid (see algorithm 1) to either the left or right at an angle drawn from a normal distribution with a mean of $32.5°$.
    - Repeat until the mean sinusoid length of the entire structure reaches 43.1μm.

Cell Attraction Dynamics

If we assume an infected KC diffuses chemokine to a downstream node α, chemokine strength at α is a function of distance:

$$\lambda / \delta$$

Where:
>λ is the chemokine strength at the infected node.
>δ is the distance in nodes between the KC and α.

Uninfected KCs are unable to modify their attraction diffusion distance from the parameterized minimum (Scenario A only), whereas infected-KC attractive chemokine diffusion distance is variable between a minimum and maximum distance. That distance is calculated as a function of the current level of attractive chemokine at the source KC location:

$$\delta = |\ \lambda \cdot (\delta\text{max} - \delta\text{min})\ |$$

Where:
>λ is the chemokine strength at the infected node.
>δmax is the maximum parameterized diffusion distance.
>δmin is the minimum parameterized diffusion distance

The function is floored to the nearest integer and that is used as the updated diffusion distance.

Cell Retention Dynamics

The equation governing NKT cell retention is:

$$\delta\text{nktleave} = \delta\text{leave}\ \ (\phi \cdot \delta\text{leave})$$

Where:
>δnktleave is the probability of an NKT cell leaving an infection site.
>δleave is the maximum parameterized retention probability.
>ϕ is the level of retentive chemokine at the infected node.

As the calculated probability will approach zero given suitable conditions, a minimum retention probability is parameterized to ensure that KCs do not become so retentive that NKT cells are then incapable of leaving.

State-Transition Diagrams

Figure S2 depicts state-transition diagrams using the Unified Modelling Language (UML). These diagrams are the engineering specific (platform) ones used to create the simulator. To improve clarity, various annotations are added to convey information relevant to our modelling context. Arrows denote transitions between states. Square brackets ([]) denote guards for a transition, conditions that must be met before a transition can occur. Dashed lines denote states or behaviours that occur concurrently. Where an assumption number is stated on a diagram, denoted by (An), refer to the relevant cell assumption table. The $\delta()$ notation denotes an interaction that might occur probabilistically, for example a cell-cell interaction.

- **Infected Kupffer Cells** (Figure S2(A)): begin in an aware state and have a minimum level of attractive chemokine and minimum diffusion distance of attraction. If the level of cell-local interferon-gamma produced by NKT cells reaches a threshold (ifnThreshold), infected KCs become engaged. When infected KCs are engaged, if there is sustained interaction with NKTs, indicated by δ(NKT), they will increase their level of attraction and retention.

- **Uninfected Kupffer Cells** (Figure S2(B)): always in an aware state and only diffuse the minimum level of attractive chemokine. They do not interact with NKTs by any other means.

- **NKT cells** (Figure S2(C)): have two state types, ActionStates and MoveStates. The initial ActionState is inactive. If an infected KC is encountered the NKT will begin producing interferon- until probabilistically leaving mediated by the retention level of the KC. If NKT cells encounter uninfected KCs, they will transition to the recovering state. NKTs leave the recovering state after a time sampled from a normal distribution, this time is significantly shorter for NKTs that previously left uninfected KCs, and hence havent been in the producing state. The default NKT cell MoveState is patrolling. Upon sensing a level of attraction, NKT cells will transition to a chemotaxing state. Interaction with an infected KC will cause the NKT to switch to an aggregating state; alternatively an uninfected KC encounter will lead back to a patrolling state. Aggregating NKT cells can transition to patrolling behavior probabilistically. Should NKT cells exit the liver environment, if the entry condition is satisfied, they will emerge from an environment entry point, effectively as another cell.

Parameterizing and Calibrating the Simulation

A full summary of the biological data available that was used to calibrate the simulation is listed in Table S1, though these are merely the domain specific parameters, and a number of implementation specific parameters are required in order to abstract domain behaviors into executable computer code. A good example of an implementation specific parameter relates to NKT cell speed. NKT cells traverse the sinusoids at 10-20m/minute. In the simulation, this corresponds to 10-20 nodes/minute. Our simulation iterations are in seconds, so for a cell to travel at a maximum speed of 20 nodes/minute it would have to move every 3 simulation iterations (p_moveMin), and a minimum speed of 10 nodes/minute every 6 simulation iterations (p_moveMax). Rather than have individual cell speed remain constant, we allow it to be dynamic within the published biological range. We calculate, probabilistically between p_moveMin and p_moveMax, the number of iterations a cell will remain stationary before its next move. This allows individual cells to speed up and slow down dynamically, yet maintains a normal distribution of cell speeds across the population and within the biologically specified range. The entire list of baseline simulation parameters can be viewed in Table S3. Several parameters have no biological equivalent though are fundamental for the implementation of many behaviors. We performed parameter sensitivity analysis (SA) in order to determine which parameters the simulation is extremely sensitive to, and to establish baseline parameter values. Finally SA allows us to ensure we are always interpreting our results with the knowledge that particular extreme parameter combinations might influence those results.

Each simulated experiment is run across 10 separate structures in order to approximate variance across the set. For each parameter value investigated (or combination of parameter values) per experiment, 500 simulation runs are performed, this number chosen after performing aleatory uncertainty analysis on the simulator. Aleatory analysis can be used to determine the minimum number of replicates runs required to both mitigate the effects of stochasticity on simulation output, and to generate results that cover a representative spectrum of possible system behaviours (Alden et al., 2013). Fig. S3f shows that 300 simulation runs per parameter combination are sufficient to have acceptable uncertainty (small variance between identical sample sizes), though we perform 500 in order to strike a balance between further reducing A-test effect size (Vargha and Delaney, 2000) and maintaining tractable simulated-experiment execution times.

Supplemental References

Haessler, U., Pisano, M., Wu, M., and Swartz, M.A. (2011). Dendritic cell chemotaxis in 3D under defined chemokine gradients reveals differential response to ligands CCL21 and CCL19. Proceedings of the National Academy of Sciences of the United States of America 108(14), 5614-5619.

Iyoda, T., Ushida, M., Kimura, Y., Minamino, K., Hayuka, A., Yokohata, S., Ehara, H., and Inaba, K. (2010). Invariant NKT cell Anergy is Induced by a Strong TCR-Mediated Signal Plus Co-stimulation. International Immunology 22(11), 905913.

Vargha, A., and Delaney, H. D. (2000). A Critique and Improvement of the "CL" Common Language Effect Size Statistics of McGraw and Wong. Journal of Educational and Behavioral Statistics 25(2), 101132.